Theoretical and experimental analysis of the aerosol assisted CVD synthesis of magnetite hollow nanoparticles

B.E. Monárrez-Cordero, P. Amézaga-Madrid, P.G. Hernández-Salcedo, W. Antúnez-Flores, C. Leyva-Porras, M. Miki-Yoshida

Abstract

Nowadays, mesoporous magnetite nanoparticles are an important class of new nanomaterials which occupy a valuable position in materials science. Owing to their several advantages over bulk magnetite and particularly with respect to higher adsorption capacity, there is a growing interest towards the use of these materials for the adsorptive removal of a variety of contaminants, including organic dyes from wastewater. Through aerosol assisted chemical vapor deposition (AACVD) technique is possible to synthesize spherical hollow nanoparticles with external diameter from 50 to 500 nm, composed of a shell of crystallites smaller than 30 nm. In the AACVD method, the structural morphology of resultant nanoparticles strongly depends on the starting precursors and operating conditions. Some advantages of this technique are the high production rate, continuous operation, use of relatively simple equipment, easy doping and the possibility to scale the process industrially. Therefore, in order to understand the formation of magnetite nanoparticles by AACVD, theoretical simulations were performed on two important steps of the synthesis: (i) temperature and carrier gas flow distribution inside of tubular reactor, and (ii) the distribution of molar concentration of the precursor in the synthesis process. Reaction kinetics of the precursor was studied to determine Arrhenius parameters. Activation energy and pre-exponential factor were calculated

experimentally from thermal analysis, these values were used in the calculation of reactants and product concentration distribution inside of the tubular reactor. Results from the simulation were compared with those obtained from the experiments.

1. Introduction

Hollow and mesoporous magnetite nanoparticles (MNPs) are being widely studied due to their outstanding and important characteristics such are particle size, high surface area, porosity, paramagnetic properties, crystallinity, high diffusion rate and reactivity. Final MNPs properties depend on crystalline phase, microstructure, particle size and morphology. Furthermore, the method of synthesis largely influences these characteristics. Finding the relation between the synthesis variables and the desired properties is a challenging task in both, nano-science and nano-technology.

All of these features make these nanoparticles be very attractive specifically for environmental applications as heavy cations removal from wastewater with removal efficiency of 70–100% and short removal time. Adsorption on this kind of particles largely depends on the overall surface area, which in turn is determined by the size of crystallites, porosity and morphology of the particle. Specific surface area of isolated crystallites is inversely related to its crystallite size (τ); since surface area of a crystallite is proportional to τ^2 and its mass to τ^3. In addition, the magnetic property of the MNPs is very important for recovering purposes from the wastewater stream, where by means of a magnetic field the MNPs are collected. Another important potential application is in the biomedicine field, where MNPs can be employed as contrast agents, drug delivery, hyperthermia, etc. In this sense,

functionalized MNPs are preferred with particle size between 10 and 30 nm. In biomedicine the magnetic property is also very important, since through a magnetic field, MNPs can be transported into the human body and focused on the organ to be treated [1]; [2]; [3]; [4] ; [5].

Additionally, it is very important to develop methodologies for producing nanoparticles at low cost and large scales. Aerosol assisted chemical vapor deposition (AACVD) technique meets these two requirements, since is a simple and easy to handle technique. This method is a variant of chemical vapor deposition technique, it is an attractive method for the preparation of nanoparticles of different materials with good characteristics and high quality. AACVD comprises three major steps: (i) generation of a cloud of droplets from the precursor solution using a nebulizer, (ii) transportation of the cloud into the reactor by means of a carrier gas, where the precursors decomposes and reacts, and (iii) the deposition and final formation of the nanoparticles. A detailed description of the technique can be found elsewhere [3] ; [6]. Recently, Monárrez-Cordero et al. [3] reported the synthesis of MNPs by the AACVD method, finding that final structure, morphology and removal properties largely depend on the processing conditions. Among these conditions, it is included the furnace temperature, carrier gas flow, nature of the precursor and diameter of the tubular reactor inside of the furnace.

Therefore, it is necessary to fully understand the phenomena occurring inside the system during the AACVD process for properly relating with the final properties developed by the nanoparticles; at the present there are few studies related with this topic.

Several numerical simulations have been performed on the process of spray pyrolysis, which have mainly focused on the conversion process from the precursor droplet into the final particle and in the effect of the evaporation of the solvent on the particles morphology. Some approaches require the use of different assumption for solving the equations of mass transfer, energy and momentum, which limits their use [7]. Tsai et al. studied the effect of the droplet size and precursor concentration on the size and morphology of the nanoparticles. They found that droplets larger than 30 μm generated by ultrasonic atomization at 120 kHz yielded hollow nanoparticles due to high solvent evaporation rate, as predicted by the conventional one particle per drop mechanism. Precursor drops 6–9 μm in diameter, generated by ultrasonic nebulizer at 1.65 MHz, yielded uniform spherical particles with proper control of precursor concentration and residence time [8].

In this work, we report the synthesis of hollow MNPs by the AACVD method at different temperatures, the microstructural characterization and the simulation of two steps in the AACVD process. Results showed that the morphology of the particles is spherical and effectively hollow, with external diameter ranging from 300 to 500 nm. Previous surface studies showed that the MNPs were mesoporous [3], with a high specific surface area. The influence of parameters like distribution of furnace temperature, carrier gas flow and the diameter of the tubular reactor, were simulated using SolidWorks – FluidWorks software. The heat flow between the furnace and the tubular reactor, as well as the heat transfer inside the tubular reactor was also simulated by this software. In addition, the reaction kinetics of the precursor were studied by thermal analysis, calculating the activation energy and

pre-exponential factors required to perform a simulation of the precursor distribution inside of the tubular reactor by the COMSOL Multiphysics software. The implemented model allows a precise examination of the impact of processing parameters and provides a solid interpretation on the development of hollow MNPs.

2. Material and methods

2.1. Synthesis of MNPs

Hollow magnetite nanoparticles (MNPs) were synthesized by the AACVD method [3] ; [6]. The starting precursor solution was a dilution of 0.05 mol dm^{-3} iron (II) Chloride tetrahydrate ($FeCl_2$ $4H_2O$) in methanol. The aerosol was carried by a mixture of Argon and air at 0.250 and 0.004 L min^{-1}, respectively. The volume ratio air:Ar was set as 0.015. Furnace temperatures tested were at 723 and 773 K. The diameter of the tubular reactor furnace was set as 15 mm.

2.2. MNPs characterization

The microstructure of the MNPs was studied in a field emission scanning electron microscope (SEM) JEOL JSM-7401F and in a high resolution transmission electron microscope (HRTEM) JEOL JEM-2200FS. The determination of particle size distribution, crystallite size and shell thickness, were performed employing a dedicated software (Digital Micrograph™ from Gatan). Particle size distribution was calculated measuring more than 500 particles, average crystallite size was determined by measuring at least 500 crystals and crust thickness was calculated by averaging more than 100 particles. Porosity of spherical nanoparticles was estimated from TEM images by measuring the quotient between the average inter-crystallite area to that of the crystallites.

Elemental analysis on the MNPs was achieved by energy dispersive X-ray spectroscopy (EDS) employing an Oxford Inca microanalysis system attached to the microscopes. Crystalline structure was analyzed by grazing incidence X-ray diffraction (GIXRD) in a Panalytical X-Pert system. Diffractions patterns were obtained using Cu Kα radiation at 40 kV and 35 mA. Diffracted beam path included a graphite flat crystal monochromator. Grazing incidence angle was fixed at 0.5°; the scanning angle (2θ) was varied from 25° to 80°, with step size of 0.02° and step time of 12 s. Average crystallite or domain size was determined according to the Scherrer equation (1):

$$\tau = \frac{K\lambda}{\beta \cos \theta}$$

In Eq. (1) τ is the average crystallite size in nm, K is a constant depending on the shape factor ($K \sim 0.9$), λ is the wave length for the incident radiation (λ = 0.15418 nm for X-rays produced from a Cu target), β is the line broadening at half the maximum intensity (FWHM) and θ is the Bragg angle.

The specific surface area was determined according to the BET method. From these characterizations, composition, morphology, particle size and crystalline structure present in the MNPs were studied as a function of the preparation conditions.

2.3. Reaction kinetics of the precursor

In the AACVD process, the decomposition of the precursor occurs in fractions of a second, making very difficult to be measured experimentally. Anyhow, it is very important to know the phenomena occurring along the process. Thus, it was

necessary to study the mechanism of the chemical reaction in the formation of the MNPs. We first used the HSC Chemistry software to test the thermodynamical feasibility of the reaction. For this purpose we used the same salt precursor in the thermal analysis. The kinetics of decomposition was carried out in a thermogravimetric analyzer (TGA) SDT Q500 from TA Instruments. Different heating rates were tried 5, 7.5, 10, 12.5, 15 and 20 K min^{-1}. A water atmosphere was used for controlling the reaction and helping to achieve the desired crystalline phase.

The kinetic constant (*k*) (Eq. (1)) can be determined from the Arrhenius law [9]:

$$K = Z \exp\left(-\frac{E}{RT}\right)$$

where k is the rate constant, Z is the frequency factor, E is the activation energy, R is the universal gas constant and T is the temperature. Thermal decomposition usually follows the Arrhenius kinetic model (Eq. (2)), proposed by Tanaka [10]:

$$\frac{d\alpha}{dt} = f(\alpha)\left[Z \exp\left(-\frac{E}{RT}\right)\right]$$

In this model, α is the fraction weight loss, T is the temperature, f(α) is a temperature independent function and t the time. Flynn and Wall [11] deduced that the activation energy has a slight deviation (Eq. (3)), when calculated from the standard Arrhenius kinetics:

$$E = -\frac{R}{b}\frac{d(\ln \beta)}{d\left(\frac{1}{T}\right)}$$

where b is a parameter dependent on E/RT and can be derive by an iterative

method from the tables provided by Flynn et al. [12]. The frequency factor (Z) can be calculated as (Eq. (4)):

$$\ln Z = \ln\left[\frac{d\alpha}{dt}\right] + \frac{E}{RT} - \ln(1-\alpha)^n$$

Where *n* is the order of the reaction.

2.4. Theoretical simulation

In order to understand determine the temperature distribution and the phenomenon of heat transfer inside the tubular reactor, the AACVD process was simulated using SolidWorks – Fluid Works software. Table 1 shows the parameters used during the simulations. On other hand, the determination of the reactants concentration inside of the tubular reactor in the AACVD process was simulated with the COMSOL Multiphysics software. Data from the parameters obtained from the kinetics of reaction, the properties of the salt precursor and carrier gas flow, were employed during the simulation. Calculations were also made of the obtained magnetite concentration and were compared with that obtained experimentally.

Table 1
Parameters used in the simulation with Solidworks – FluidWorks. Temperature of the tubular furnace 723 K.

Pipe diameter (mm)	Ar flow ($cm^3\ min^{-1}$)	Air flow ($cm^3\ min^{-1}$)
9	1000	15
9	250	4
9	125	2
15	2000	30
15	1000	15
15	500	8
15	250	4

3. Results and discussion

3.1. MNPs microstructure and characterization

Fig. 1(a) and (b) shows secondary electrons SEM images. From these images we can observe the formation of typical agglomerated particles with hollow spherical morphology. Fig. 1a shows MNPs synthesized at 723 K, the average particle size measured from several micrographs gave 300 ± 78 nm, while those synthesized at 773 K (Fig. 1b) presented an average diameter of 380 ± 100 nm. Both samples were synthetized under the same conditions of carrier gas flow and inside a vycor tubing reactor of 15 mm in diameter. Overall, at these operation parameters, a regular morphology is observed everywhere in the tubular reactor. Results of the average particle diameter, crust thickness and crystallite size measurements performed from the SEM images are presented in Table 2. Spheres were composed of hundreds of small crystallites which increased in size with temperature of synthesis (see Table 2). Thus, crystallites synthesized at 773 K were bigger than those at lower temperature. Previous results have shown the effect of the diameter of the tubular reactor on the size of the MNPs, finding smaller particles and crystallite size in a tube with 9 mm in diameter [3]. This corroborates the influence of the diameter of the tubular reactor on both sphere and crystallite size. Thus, if smaller sizes are required e.g. for biomedicine applications a smaller diameter in the tubular reactor must be used in order to reduce the residence time.

In addition, the elemental composition of the MNPs was analyzed by EDS. Results showed a very homogeneous composition since only signals from iron and

oxygen were found; it is worthwhile to mention that in particular chlorine signal was not detected. Atomic ratio of iron to oxygen (Fe/O) was very close to the stoichiometric concentration. Another factor that contributes to the size is the concentration of the precursor solution. At a higher concentration more dense MNPs were formed [3], i.e. the crust layer was thicker and crystallites were larger. These results indicate that the AACVD technique is suitable for preparing homogeneous and high purity hollow nanoparticles in one single step. Besides, porosity in MNPs was generated during the synthesis without the need of employing templates or very specialized reagents. This is a great advantage over other techniques such are sol–gel synthesis and chemical precipitation method, where several byproducts are generated. Calculations were made to determine the size of a sphere considering the size of the drop that is formed when the precursor is nebulized. Calculations indicate that one drop of 2.2 μm can generate one sphere of 300 nm, with a crust thickness of 26 nm and 30% of porosity for a synthesis temperature of 723 K. When the temperature was increased to 773 K, particles showed the same morphology but larger dimensions in size and in crystallite size (380 nm and 25 nm respectively). These results are shown in Table 3, where we can also see the percent porosity of the synthesized MNPs at the two temperatures. MNPs presented higher porosity synthesized at 773 K, this property is due since the increase of crystallite size generate the increase of crystallite spacing. Fig. 2(a) and (b) shows bright field TEM images of single hollow spheres synthesized at 723 K and 773 K, respectively, it can be seen almost perfect spherical nanostructures composed of many small crystallites. With those images we could corroborate the average size of particle and

crystallites observed in SEM images. Fig. 3 shows XRD patterns from polycrystalline MNPs synthesized at different temperatures. Diffraction peaks indexation corresponded mainly to the magnetite phase (Fe_3O_4) and a small amount of iron (III) oxide (Fe_2O_3) [13]. The strong and sharpen peaks confirmed that samples are well crystallized. Specific surface area determination showed a value of 66 $m^2\ g^{-1}$ for sample synthesized at 723 K, and 47 $m^2\ g^{-1}$ for sample synthesized at 773 K, both synthesized in the 15 mm diameter tubular reactor. For comparison purposes, in a previous work [3] a 9 mm diameter tubular reactor was employed for synthesizing the MNPs at 723 K and the determined specific surface area was 72 $m^2\ g^{-1}$. This difference is explained in terms of the crystallite size, where in the previous work crystallite size was smaller than in the present work. These values are reported in Table 2. The difference in the specific surface area is caused by the increased size of MNPs synthesized at higher temperature and the change in the diameter of the tubular reactor, which in turn increases the residence time of the particle inside the reactor. Anyhow, the values of the specific surface area determined in this work can be considered as optimal for removal of heavy metals applications when compared to other type of particles with similar morphology and size [14] ; [15]. It is

worthwhile to remark that theoretical specific surface area of

Table 2
Specific and theoretical specific surface area; average diameters of particle, crystallites and crust thickness using a vycor tube as a tubular reactor of 15 mm of diameter, in an AACVD process and comparing the results with previous work from Monárrez-Cordero et al. [3].

Temperature (K)	Tubular reactor diameter (mm)	Average particle diameter (nm)	Average crust thickness (nm)	Average crystallites size (nm)	Specific surface area ($m^2 g^{-1}$)	Theoretical specific surface area ($m^2 g^{-1}$)
723	15	300 ± 78	26 ± 9	19 ± 5	66	63
773	15	380 ± 100	27 ± 5	25 ± 6	47	48
723	9 [3]	280 ± 10	20 ± 3	15 ± 5	72	80

Table 3
Data used to calculate the number of sphere obtained and the number of crystallites formed in one sphere, considering the size of the drop.

Synthesis temperature (K)	Drop diameter (μm)	Crystallites formed from one drop	Calculated porosity (%)
723	2.2	1308	30
773	2.2	578	59

isolated spherical crystallites with diameter equal to the experimental average crystallite size agrees well to the measured surface area; then it can be concluded that in the actual microstructure of the hollow spherical MNPs the crystallites perform as isolated spherical nanoparticles in regard to its surface area, fact that is very advantageous to many surface related applications.

3.2. Simulation of the distribution temperature and gas carrier flow inside of tubular reactor

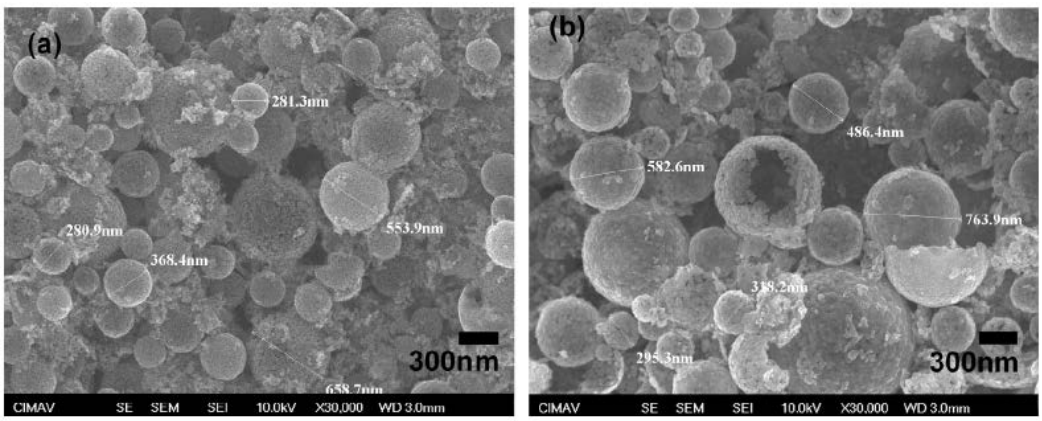

Fig. 1. (a and b) SEM images of MNPs, at 0.05 M; synthesized at 673 K (1a) and 773 K (1b), with an Ar-air mixture flow of 250 L min^{-1} and 4 L min^{-1} respectively.

SolidWorks – FluidWorks software was used to simulate the temperature distribution inside the furnace and the heat transfer across the wall of the tubular reactor, evaluating the effect of the carrier gas flow. Fig. 4a shows the temperature profile along the furnace and vycor tubing near to the gas entrance. In this figure, it is observed a sharp increase of the temperature, reaching the setting point temperature of the furnace very quickly. As expected, temperature at the initial and ending zones of the furnace was lower than in the center. Heat transfer towards the tubular reactor was efficient along the furnace, since the nominal temperature of the furnace was also reached by the gas carrier. In the center of the tubular reactor, temperature is slightly lower, consistent with the higher carrier gas velocity. These simulated results were congruent with those measured experimentally see Fig. 4b.

Velocity of the carrier gas inside of the tubular reactor is shown in Fig. 4c. It was observed that carrier gas velocity was lower next to the walls of the tubular reactor, while it was maxima at the center of the tube;

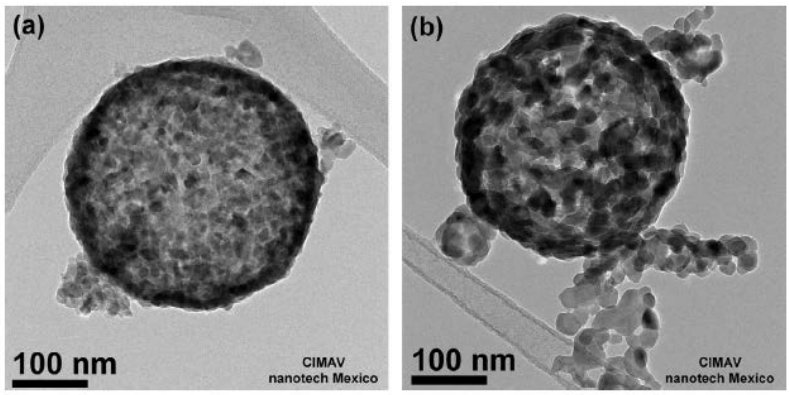

Fig. 2. (a and b) TEM images of MNPs, at 0.05 M; sinthetized at 673 K (1a) and 773 K (1b), with an Ar-air mixture flow of 250 L min^{-1} and 4 L min^{-1} respectively.

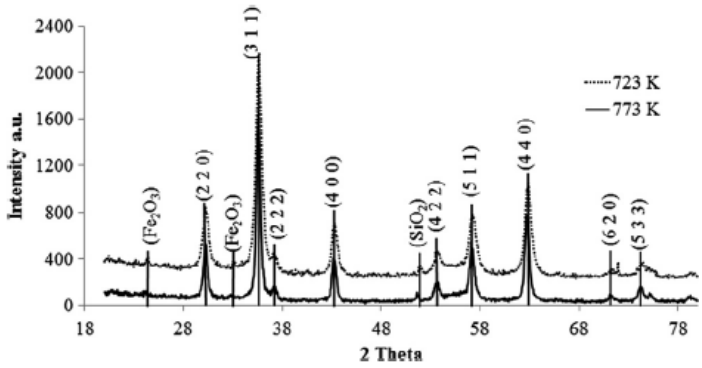

Fig. 3. GIXRD patterns from MNPs synthesized at different temperatures.

this is a normal behavior for a laminar viscous fluid inside a tube. When temperature was increased, calculated gas flow increased as well. Additional simulations were performed with tubing diameter of 9 mm, finding qualitatively similar results than those with a larger diameter.

3.3. Chemical kinetic mechanism

After proposing several reaction paths and using the HSC software to verify its thermodynamic feasibility, the following reaction was obtained:

$$6FeCl_2*4H_2O+O_2(g)\rightarrow 2Fe_3O_4+12HCl(g)+18H_2O(g)$$

Fig. 5 shows the high temperature range (>723 K) of the weight change of the salt precursor at different heating rates. In general, the decomposition behavior was similar regardless the heating rate. In the low temperature range (not shown), between 473 K and 673 K the precursor dehydrates. Over this temperature, chlorine evolved. In the range of 723–1100 K there are several weight losses corresponding to the decomposition of $FeCl_2$ and oxidation of the iron, and the further formation of the magnetite. From Fig. 5 it is observed that at lower heating rates (5 and 7.5 K min^{-1}),

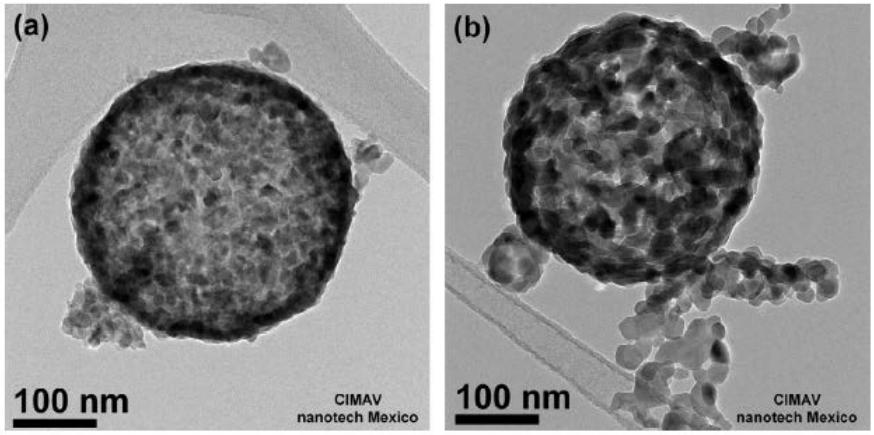

Fig. 2. (a and b) TEM images of MNPs, at 0.05 M; sinthetized at 673 K (1a) and 773 K (1b), with an Ar-air mixture flow of 250 L min^{-1} and 4 L min^{-1} respectively.

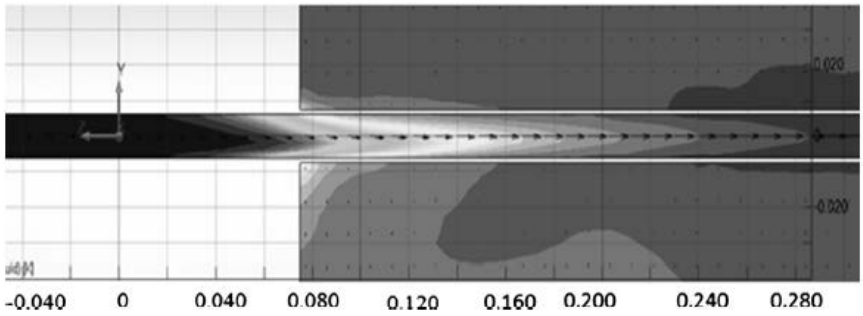

Fig. 4a. Distribution of the temperature simulated by Solidworks software.

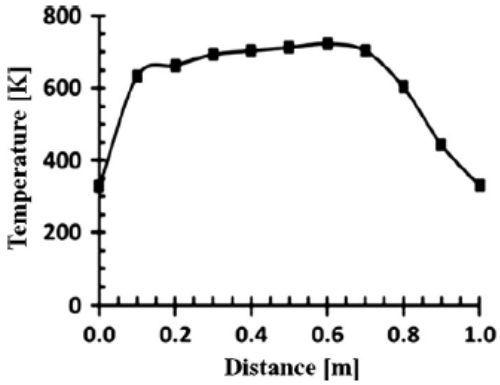

Fig. 4b. Experimental distribution of temperature inside the furnace.

the weight loss is carried out more slowly, this is because when the heating is slower provides greater opportunity to respond to changes generated in the reaction system. In this way, diffusion problems are diminished and a better reaction is carrier

out. In contrast, at higher heating rates (10 and 20 K min^{-1}) chemical reaction is carried out much faster, showing a more stepped thermal decomposition. Anyway, magnetite was produced at every heating rate. The data calculated thermodynamics by HSC software are showed in Table 4. As observed in that table, the calculated value for the Gibbs free energy was −166 kJ and this value diminished with temperature. These data allow us to know that the proposed chemical reaction is feasible to proceed at the given experimental conditions.

3.3.1. Calculation of the Arrhenius parameters

The kinetics reaction of the salt precursor was calculated from TGA measurements using a dynamic method with different heating rates. The calculated values of the pre-exponential factor was calculated as 1.38×10^7 $m^3/(mol\ s)$, and the value of activation energy was 159 kJ mol^{-1}. These values were calculated after finding the best fitting linear model accordingly to Flynn and Ozawa [11] ; [12]. Fig. 6 shows the linear fitting at different weight losses, starting from the dehydrated iron chloride. The best fitting was found at a weight loss of 30%, and this was employed in the calculation of the activation energy. With the calculated data, it was observed

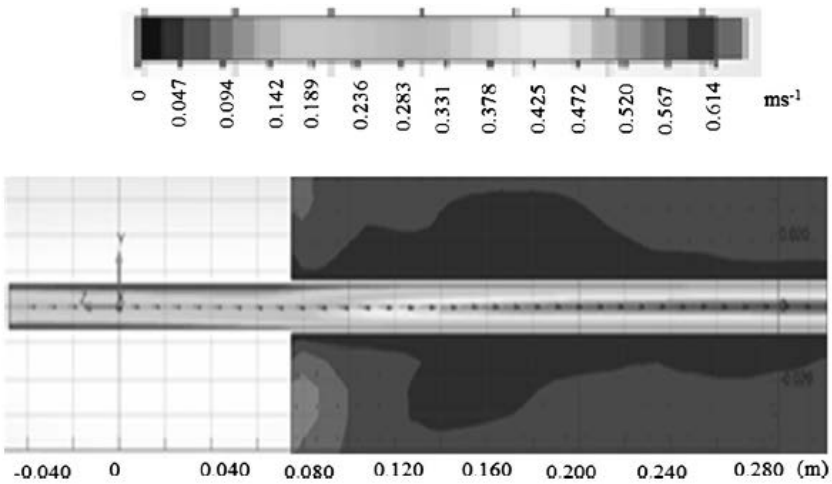

Fig. 4c. Distribution of the gas carrier flow rate inside substrate simulated by Solidworks software.

Table 4
The data calculated thermodynamics by HSC Chemistry software. The calculated value for the Gibbs free energy was −166 kJ and this value diminished with temperature.

T (K)	ΔS (kJ)	ΔS (JK^{-1})	ΔG (kJ)
273	1638	4311	461
323	1609	4212	248
373	1582	4134	40
423	1556	4069	−166
473	1531	4014	−368
523	1508	3967	−567
573	1485	39,258	−765
623	1464	3891	−960
673	1445	3861	−1154
723	1428	3836	−1346
773	1413	3817	−1537
823	1401	3802	−1728
873	1389	3787	−1918
923	1374	3770	−2107
973	1359	3754	−2295
1023	1344	3739	−2482
1073	1329	3725	−2669
1123	1315	3712	−2855

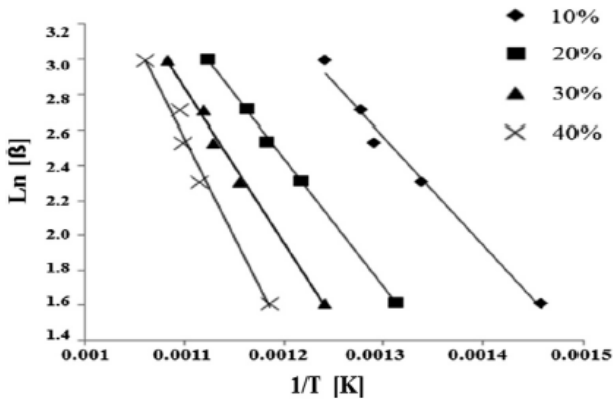

Fig. 6. Linear fit by the method Flynn–Wall–Ozawa of the data obtained by thermogravimetric analysis.

that the activation energy diminished as the weight loose decreased. Extrapolating these results into AACVD process means that during an accelerated heating, the spherical and hollow MNPs are formed as a result of the rapid droplet evaporation and the fast rate decomposition of the salt. Under these processing conditions, this type on MNPs requires a less activation energy.

Conversely, if the heating rate is slow, the system takes longer to raise the temperature and energy requirements are higher for the reactions to occur.

3.4. Theoretical simulation of the distribution of the reactants and product concentration inside of the tubular reactor

Thermodynamic data obtained were used to simulate the distribution of reactant ($FeCl_2$) and product (magnetite) inside of the tubular reactor by COMSOL Multhiphysics Software. Table 5 defines the variables and mathematical expressions employed in this calculation. In the table, it is described the variables for a first order reaction (*xA*, *cB*, *cC* and *rA*), the axial velocity of the flow inside the tubular reactor (*Uz*), heat flow (*Q*) and the temperature variation along the tubular reactor (*Ttb*). Once having the equations governing the process, data were obtained to carry out the simulation. This data is presented in Table 6. The calculated molar flow from the simulations was 1.87×10^{-4} mol h^{-1}, while that obtained experimentally was 2.73×10^{-5} mol h^{-1}. This results are can be

Table 6
Equations and variables used in the simulation by COMSOL Multhiphysics Software.

Variables name	Expression	Description
Uz	$2 * u0 * (1-(r/R)^2)$ (m s^{-1})	Axial flow velocity
xA	$(cA0-cA)/cA0$	Conversion of species
cB	$cB0-2/3 * cA0 * xA$ (M m^{-3})	Concentration of species
cC	$1/3 * cA0 * xA$ (M m^{-3})	Concentration of species
cD	$cA0 * xA$ (M m^{-3})	Concentration
rA	$-A * \exp(E/(Rg * T)) * (cA * cB)$ ($M/(m^3 s)$)	Reaction rate
Q	$(-rA) * (-dHRx)$ (w m^{-3})	Heat production
Ttb	$Tm * \cos((z\text{-}L/2)/(L/2) * (\text{pi}/7))$ (K)	Substrate temperature

considered in well agreement with experiments. These results suggest that other parameters can be varied in the simulations and keep finding reliable results. The results found from the simulation of the precursor concentration are shown in Fig. 7. It is observed that the initial concentration of 0.196 mol m^{-3} reduces very quickly to 0.187 mol m^{-3}. This values remains until the final MNPs are obtained.

4. Conclusions

High purity, mesoporous hollow magnetite nanoparticles were synthesized by AACVD technique. Microstructural characteristics strongly depend on the synthesis conditions. Studying these conditions was helpful for understanding their effect on the structure and surface area of the MNPs. Specific surface area of hollow spherical particles was found in close agreement to that calculated for isolated spherical crystallite with diameter equal to the average crystallite size determined experimentally. This means that the porous microstructure of the hollow spherical MNPs makes that the component crystallites perform as isolated spherical nanoparticles in regard to surface related phenomenon. Then hollow spherical MNPs of this work have advantageous characteristics due to its assembled crystallites microstructure concerning to particle manipulation or recollection and, on the other side, the component crystallites perform as isolated nanoparticles with regard to their specific surface area. Numerical simulation of temperature distribution and carrier gas flow was performed. Thermogravimetric analyses of $FeCl_2$ precursor and numerical simulation permitted to calculate concentration distribution of reactants and products inside of the tubular reactor.

Acknowledgements

The authors would like to thank E. Torres-Moye, K. Campos-Venegas, C. Ornelas, L.de la Torre-Sáenz, D. Lardizabal, O. Solís-Canto, M. Lugo-Ruelas, O. Esquivel-Pereyra, G. Rivas-Amézaga, for their technical assistance.

References

[1] D.K. Kim, M. Mikhaylova, F.H. Wang, J. Kehr, B. Bjelke, Y. Zhang, T. Tsakalakos, M.Muhammed, Starch-coated superparamagnetic nanoparticles as MR contrast agents, Chem. Mater. 15 (2003) 4343–4351.

[2] A.K. Gupta, S. Wells, Surface-modified superparamagnetic nanoparticles for drug delivery: preparation, characterization, and cytotoxicity studies, IEEE Trans. Nanobiosci. 3 (2004) 66–73.

[3] B. Monárrez-Cordero, P. Amézaga-Madrid, W. Antúnez-Flores, C. Leyva-Porras,

P. Pizá-Ruiz, M. Miki-Yoshida, Highly efficient removal of arsenic metal ions with high superficial area hollow magnetite nanoparticles synthetized by AACVD method, J. Alloys Comp. 586 (2014) S520–S525.

[4] M. Abhijit, D.G. Sunando, K.B. Jayant, D. Sirshendu, Adsorption of arsenite using natural laterite as adsorbent, Sep. Purif. Technol. 55 (2007) 3–8.

[5] T. Tuutijärvi, J. Lub, M. Sillanpää, G. Shen, As (V) adsorption on magnetite nanoparticles, J. Hazard Mater. 166 (2009) 1415–1420.

[6] H.E. Esparza-Ponce, A. Reyes-Rojas, W. Antúnez-Flores, M. Miki-Yoshida, Synthesis and characterization of spherical calcia stabilized zirconia nano-powders obtained by spray pyrolysis, Mater Sci. Eng. A343 (2003) 82–88.

[7] D.H. Charlesworth, W.R. Marshall Jr., Evaporation from drops containing dissolved solids, J. AIChE 6 (1960) 9–23.

[8] S.C. Tsai, Y.L. Song, C.S. Tsai, C.C. Yang, W.Y. Chiu, H.M. Lin,

Ultrasonic spray pyrolysis for nanoparticles synthesis, J. Mater. Sci. 39 (2004) 3647–3657.

[9] Levenspiel, Chemical Reaction Engineering, eighth ed., Reverte, Barcelona, 1986. pp. 3–44.

[10] H. Tanaka, Thermal analysis and kinetics of solid state reactions, Thermochim. Acta 267 (1995) 29–44.

[11] J. Opfermann, E. Kaisersberger, An advantageous variant of the Ozawa–Flynn–Wall, Anal. Thermchim. Acta 203 (1992) 167–175.

[12] J.H. Flynn, L.A. Wall, A. Quick, Direct method for the determination of activation energy from thermogravimetric data, Polym. Lett. 4 (1966) 323–328.

[13] Joint committee on powder diffraction standards, powder diffraction file, in: International Center for Diffraction Data, Swarthmore, PA, 2006. Card 00–088-0315.

[14] K. Simeonidis, T. Gkinis, S. Tresintsi, C. Martinez-Boubeta, G. Vourlias, I. Tsiaoussis, G. Stavropoulos, M. Mitrakas, M. Angelakeris, Magnetic separation of hematite-coated Fe3O4 particles used as arsenic adsorbents, J. Chem. Eng. 168 (2011) 1008–1015.

[15] Z. Huang, F. Tang, Preparation, structure, and magnetic properties of mesoporous magnetite hollow spheres, J. Colloid Interface Sci. 281 (2005) 432–436.